LIMIT-CYCLE OSCILLATIONS IN HIGH-ASPECT-RATIO WINGS[†]

M. J. Patil, D. H. Hodges

School of Aerospace Engineering, Georgia Institute of Technology
Atlanta, GA 30332, U.S.A.

AND

C. E. S. Cesnik

Department of Aeronautics and Astronautics, Massachusetts Institute of Technology
Cambridge, MA, U.S.A.

The paper presents results obtained for limit-cycle oscillations (LCOs) in high-aspect-ratio wings caused by structural and aerodynamic nonlinearities. The analysis is based on geometrically exact structural analysis and finite-state unsteady aerodynamics with stall. The results indicate that stall limits the amplitude of post-flutter unstable oscillations. At speeds below the linear flutter speed, LCOs can be observed if the stable steady state is disturbed by a finite-amplitude disturbance. A critical disturbance magnitude is required at a given speed and a critical speed is required at a given disturbance magnitude to initiate LCOs. The LCO initiation mechanism can be attributed to the change in structural characteristics of the wing with deformation. It is also observed that the LCO gets increasingly complex with increasing speed. Period doubling is observed at low speeds and as the speed increases the oscillations lose periodicity and become chaotic.   © 2001 Academic Press

1. INTRODUCTION

THE LINEAR THEORY OF STABILITY, when applied to aeroelasticity problems, typically leads to a set of eigenvalues. It predicts that small disturbances applied to a system at an unstable equilibrium grow exponentially. Within its valid range, linear theory is correct, i.e., *small* disturbances *do* grow exponentially—at least *at first*. However, one should not regard the results of linear theory to have any significance whatsoever regarding the behavior of a system subjected to large disturbances, or after a long time elapses from an initial small disturbance. For example, according to linear theory the response of an unstable system will diverge from the unstable equilibrium to infinity (or material failure). This does not always comport with experimental evidence, and nonlinear analysis methodology has been developed to remedy this problem (Nayfeh & Mook 1979).

If a system has a nonlinear stiffening term, then in most occasions the amplitude of oscillations will grow until a LCO is reached. LCOs, though stable in the sense of Lyapunov, are not asymptotically stable. That is, although the final state is bounded, the

---

[†] Presented as paper AIAA-99-1464 at the 40th Structures, Structural Dynamics and Materials Conference, St. Louis, Missouri, April 12–15, 1999.

system will not asymptotically approach its original equilibrium state as time grows. Moreover, a LCO is not necessarily the result of a linear instability. LCOs can be induced by certain disturbances, if sufficiently large, even when the given equilibrium state is stable. Basically, if the disturbances are not small, then the response cannot be predicted by linear theories. Depending on the amplitude of the LCO, the structure may or may not experience immediate failure. However, for an aircraft, LCOs pose significant problems in their own right. The vibration caused by LCOs causes fatigue, reducing the useful life of the structure. Thus, efficient prediction of LCOs is very important during design, especially for aircraft flying near the limits of the assumptions behind linear theory.

Theoretical investigation of parameters affecting LCOs in an aircraft is a difficult task, even for very low-order systems. The investigation of a realistic wing with an accurate representation of the aerodynamics leads to a very computationally intensive task. Presently, computational methods which simulate the system behavior are used to obtain time histories of motion, which are then used to study any observed LCO. It is necessary to investigate LCO in the best possible way so as to get a deeper understanding of its initiation and sustaining mechanisms.

There are two main motivating factors for the present study, (i) to investigate LCO in a high-aspect-ratio composite (highly flexible) wing, like those to be used in future high-altitude long-endurance unmanned aerial vehicles, using time response analysis, and, (ii) to investigate mechanisms responsible for initiating and sustaining LCOs.

2. BACKGROUND

There are various modalities to analyze and predict limit-cycle oscillations. Given below are several which have been recently applied to aeroelastic LCO study.

The most common way of analyzing LCOs is via time-marching. The system is simulated in time for various initial conditions. And the response is plotted in time or as a phase-plane plot to see if (i) the response is diverging and (ii) it converges to a LCO. This method is computer time intensive and one needs to select a set of initial conditions relevant to the problem at hand. Tang *et al.* (1998) used a reduced-order, finite-state inflow model to analyze the nonlinear behavior of airfoil sections with free-play nonlinearities. Tang & Dowell (1993) have analyzed the nonlinear behavior of a flexible rotor blade due to structural, free-play and aerodynamic stall nonlinearities. The analytical results were compared with experimental observations. In both cases time-marching was used. Patil & Hodges (1998a) have presented results on the LCO observed in stiff metallic wings. Finite elements in space and time were used for time integration.

In harmonic balance analysis the response is assumed to be a linear combination of a set number of harmonics. The solution is obtained by solving the nonlinear algebraic equations associated with all the harmonics. This type of analysis can often be improved by taking a larger number of harmonics. Unfortunately, it is not always possible to write the nonlinearities in terms of a set of harmonics, and even if it is, it may be too cumbersome. Dunn & Dugundji (1992) used Fourier analysis to extract the relevant harmonics from the ONERA dynamic stall model and then used the harmonic balance method to predict LCOs in a plate-like composite wing. The results obtained were compared with experimental data. Use of the harmonic balance method for spatially continuous nonlinear problems (flexible wings) needs to be investigated.

Wavelet filtering is a technique still under development. It involves transforming the time histories into a time–frequency domain through a wavelet filter which calculates the Fourier components at various time steps. It is only a filtering (rather than analysis) technique and thus can take time histories from either experimental data or computation. It is useful in

prediction of the onset of LCOs. This analysis has been proposed by Lind *et al.* (1998) and has been used successfully to predict LCO using the nonlinear airfoil response data generated by O'Neil & Strganac (1996).

The experimental data obtained by O'Neil & Strganac (1996) is for an airfoil on a nonlinear support system. A later theoretical analysis using the method of multiple scales by Gilliatt *et al.* (1998) includes nonlinearities due to stall in a quasi-steady way. The objective is to predict internal resonance in such a model and to explore its effect as a LCO triggering mechanism.

3. AEROELASTIC MODEL

The aeroelastic model used in the present analysis is based on (i) a mixed variational formulation that employs exact intrinsic equations for dynamics of beams in a moving frame (Hodges 1990) and (ii) a finite-state airloads model for deformable airfoils on fixed and rotating wings (Peters & Johnson 1994; Peters *et al.* 1995). The structural theory is a nonlinear intrinsic formulation for the dynamics of initially curved and twisted beams. There are no approximations to the geometry of the reference line of the deformed beam or to the orientation of the cross-sectional reference frame of the deformed beam. A compact mixed variational formulation can be derived from these equations which is well-suited for low-order beam finite element analysis based in part on the paper by Hodges (1990). The aerodynamic theory consists of a state-space theory for the lift, drag, and all generalized forces of a deformable airfoil. Trailing-edge flap deflections are included implicitly as a special case of generalized deformation. The theory allows for a thin airfoil which can undergo arbitrary small deformations with respect to a reference frame which can perform arbitrarily large motions.

Coupling the structural and aerodynamics models one gets the complete aeroelastic model. Finite elements in space and time are used to march in time and get the dynamic nonlinear behavior of the system. The formulation is given in detail in an earlier paper (Patil *et al.* 1998*b*) and is presented here briefly so as to give the readers a flavor of the underlying theory.

The formulation is based on equations derived from Hamilton's principle, which can be written as (Hodges 1990)

$$\int_{t_1}^{t_2} [\delta(K - U) + \overline{\delta W}] \, dt = \overline{\delta A}, \tag{1}$$

where K and U are the kinetic and potential (strain) energy, respectively, $\overline{\delta W}$ and $\overline{\delta A}$ are the virtual work and virtual action terms, and t_1 and t_2 are the limits of the time interval over which the solution is required.

The variation of the kinetic and potential energy for the wing can be expressed as

$$\delta K = \int_0^\ell \left[\delta V^T \left(\frac{\partial K}{\partial V} \right)^T + \delta \Omega^T \left(\frac{\partial K}{\partial \Omega} \right)^T \right] dx, \tag{2}$$

$$\delta U = \int_0^\ell \left[\delta \gamma^T \left(\frac{\partial U}{\partial \gamma} \right)^T + \delta \kappa^T \left(\frac{\partial U}{\partial \kappa} \right)^T \right] dx, \tag{3}$$

where V and Ω are the vectors of linear and angular velocities, and γ and κ are the strain and curvature vectors.

Now, the momentum and force variables are defined as

$$\left\{\begin{matrix} P \\ H \end{matrix}\right\} = \left\{\begin{matrix} \dfrac{\partial K^{\mathrm{T}}}{\partial V} \\ \dfrac{\partial K^{\mathrm{T}}}{\partial \Omega} \end{matrix}\right\} = \begin{bmatrix} m & -m\tilde{\bar{\xi}} \\ m\tilde{\bar{\xi}} & I \end{bmatrix} \left\{\begin{matrix} V \\ \Omega \end{matrix}\right\}, \tag{4}$$

$$\left\{\begin{matrix} F \\ M \end{matrix}\right\} = \left\{\begin{matrix} \dfrac{\partial U^{\mathrm{T}}}{\partial \gamma} \\ \dfrac{\partial U^{\mathrm{T}}}{\partial \kappa} \end{matrix}\right\} = [\mathscr{S}] \left\{\begin{matrix} \gamma \\ \kappa \end{matrix}\right\}, \tag{5}$$

where P and H are the linear and angular momentum components in the deformed-beam reference frame, and F and M are the internal force and moment components in the deformed-beam reference frame; m, $\tilde{\bar{\xi}}$ and I are the mass per unit length, mass offset and moment of inertia matrix, respectively, which together define the inertial property of the cross-section, while $[\mathscr{S}]$ is the cross-sectional stiffness matrix. The equations given above are the linear constitutive laws relating velocity variables to momentum variables and strain variables to force variables.

The variation of the generalized velocity and strain measures can be expressed in terms of virtual displacement ($\overline{\delta q}$) and virtual rotation vectors ($\overline{\delta \psi}$) (Hodges 1990) as

$$\delta V = \dot{\overline{\delta q}} + \tilde{\Omega}\,\overline{\delta q} + \tilde{V}\,\overline{\delta \psi}, \qquad \delta \Omega = \dot{\overline{\delta \psi}} + \tilde{\Omega}\,\overline{\delta \psi}, \tag{6, 7}$$

$$\delta \gamma = \overline{\delta q}' + (\tilde{k} + \tilde{\kappa})\overline{\delta q} + (\tilde{e}_1 + \tilde{\gamma})\overline{\delta \psi}, \qquad \delta \kappa = \overline{\delta \psi}' + (\tilde{k} + \tilde{\kappa})\overline{\delta \psi}. \tag{8, 9}$$

Finally, the virtual work done by applied external (aerodynamic) forces (f_a) and moments (m_a) is given by

$$\int_0^{\ell} (\overline{\delta q}^{\mathrm{T}} f_a + \overline{\delta \psi}^{\mathrm{T}} m_a)\, \mathrm{d}x. \tag{10}$$

Now, one can write down the weak form of the Hamilton's principle as

$$\int_{t_1}^{t_2} \int_0^{\ell} \left\{ (\dot{\overline{\delta q}}^{\mathrm{T}} - \overline{\delta q}^{\mathrm{T}} \tilde{\Omega} - \overline{\delta \psi}^{\mathrm{T}} \tilde{V})\, P + (\dot{\overline{\delta \psi}}^{\mathrm{T}} - \overline{\delta \psi}^{\mathrm{T}} \tilde{\Omega})\, H [(\overline{\delta q}')^{\mathrm{T}} - \overline{\delta q}^{\mathrm{T}} (\tilde{k} + \tilde{\kappa}) \right.$$

$$\left. - \overline{\delta \psi}^{\mathrm{T}} (\tilde{e}_1 + \tilde{\gamma})]\, F - [(\overline{\delta \psi}')^{\mathrm{T}} - \overline{\delta \psi}^{\mathrm{T}} (\tilde{k} + \tilde{\kappa})]M + \overline{\delta q}^{\mathrm{T}} f_a + \overline{\delta \psi}^{\mathrm{T}} m_a \right\} \mathrm{d}x\, \mathrm{d}t$$

$$= \int_0^{\ell} (\overline{\delta q}^{\mathrm{T}} \hat{P} + \overline{\delta \psi}^{\mathrm{T}} \hat{H})\Big|_{t_1}^{t_2} \mathrm{d}x - \int_{t_1}^{t_2} (\overline{\delta q}^{\mathrm{T}} \hat{F} + \overline{\delta \psi}^{\mathrm{T}} \hat{M})\Big|_0^{\ell} \mathrm{d}t, \tag{11}$$

where the hatted quantities are the space–time boundary values of the indicated quantities stemming from the virtual action term.

One can integrate the above equation by parts; thus, transferring the temporal and spatial derivatives from the virtual displacements and rotations to the generalized momenta and force variables, and leading to the exact intrinsic equations as given in Hodges (1990). These equations must be supplemented with kinematic (strain–displacement and velocity–displacement) and constitutive (force–strain and momentum–velocity) equations to form a complete set of equations. Then these equations can be collected together to form a set of nonlinear differential-algebraic equations in time. They can also be used to form nonlinear

steady-state equations for calculating the steady or static solution, and can be linearized about the nonlinear steady state to obtain a set of perturbation equations.

On the other hand, the above variational statement is in its weakest form in space as well as time and is a suitable candidate for space–time, finite-element discretization for time-marching. To do so, the formulation is first converted to a form which leaves the generalized speeds, strains, forces, momenta and displacements as independent variables in a single variational statement. This is done by adding the kinematical and constitutive equations as constraints to the variational statement using Lagrange multipliers.

The constitutive equations were given earlier. The kinematic equations are given by

$$V = C_w C_b [\dot{u} + v + \tilde{\omega}(r + u)], \tag{12}$$

$$\Omega = C_b \left(\frac{\Delta - \frac{1}{2}\tilde{\theta}}{1 + \frac{1}{4}\theta^T\theta} \right) \dot{\theta} + C_w C_b \omega, \tag{13}$$

$$\gamma = C_w C_b (C_b^T e_1 + u') - e_1, \tag{14}$$

$$\kappa = C_b \left(\frac{\Delta - \frac{1}{2}\tilde{\theta}}{1 + \frac{1}{4}\theta^T\theta} \right) \theta', \tag{15}$$

where u and θ are the displacements and Rodrigues parameters (representing the rotation) of the beam, respectively, Δ denotes the identity matrix, and ($\tilde{}$) represents the dual matrix of the corresponding vector. C_b and C_w are the direction cosine matrices; C_b relates the wing root and the undeformed wing cross-section frame, while C_w relates the wing undeformed and deformed frames. The above kinematical equations along with the constitutive equations are added as constraint in the variational principle.

Before proceeding to the final variational statement, it is necessary to account for aerodynamic forces since the problem under consideration is that of aeroelastic response. The aerodynamic forces are the external forces acting on the wing. The aerodynamic model used is that of Peters & Johnson (1994) and Peters et al. (1995). The theory gives the unsteady aerodynamic forces on an airfoil section in terms of the inflow. The aerodynamic loads used are as described in detail in Peters & Johnson (1994). The airloads are given in terms of the Glauert expansion coefficients of aerodynamic loads perpendicular to the airfoil (L_n) as

$$\frac{1}{2\pi\rho} \{L_n\} = -b^2 [M] \{\dot{v}_n\} - bu_0 [C - G] \{v_n - \lambda_0\}, \tag{16}$$

where u_n and v_n are the Glauert coefficients of the airflow relative to the airfoil parallel and perpendicular to the airfoil, and ρ, b are the air density and semichord, respectively. The matrices denoted by $[M]$, $[C]$, $[G]$ are constant matrices whose expressions are given in Peters & Johnson (1994). The required airloads are obtained as a linear combination of L_n.

The inflow (λ) on the other hand is modeled by a set of differential equations at each span-wise station. The ordinary differential equations are again derived from the integro-differential airloads equations through a Glauert expansion. The inflow is thus represented by a finite-state theory (Peters et al. 1995). The inflow coefficients (λ_0) is represented in terms of N states $\lambda_1, \lambda_2, \ldots, \lambda_N$ as

$$\lambda_0 \approx \frac{1}{2} \sum_{n=1}^{N} b_n \lambda_n, \tag{17}$$

where the b_n are found by use of the least-squares method, and the λ_n are obtained by solving a set of N first-order differential equations as

$$[A] \{\dot{\lambda}\} + \{\lambda\} = \{c\} \bar{\Gamma}, \tag{18}$$

where $\bar{\Gamma}$ is the normalized circulation $\Gamma/(2\pi b)$. The expression for the normalized circulation can be shown to be

$$\bar{\Gamma} = \{1\}^{\mathrm{T}}[C - G]\{v_n - \lambda_1\}. \tag{19}$$

Adding all the constraints to the Hamilton's variational statement and converting the expanded Hamilton's principle to the weakest form, i.e., transferring any remaining spatial or temporal derivatives from the variables to the test functions (virtual displacement or variations of Lagrange multipliers) we have

$$
\begin{aligned}
\int_{t_1}^{t_2} \int_0^\ell \Big\{ & (\dot{\overline{\delta q}}^{\mathrm{T}} - \overline{\delta q}^{\mathrm{T}}\tilde{\Omega}^* - \overline{\delta\psi}^{\mathrm{T}}\tilde{V}^*)P + (\dot{\overline{\delta\psi}}^{\mathrm{T}} - \overline{\delta\psi}^{\mathrm{T}}\tilde{\Omega}^*)H - [(\overline{\delta q}')^{\mathrm{T}} - \overline{\delta q}^{\mathrm{T}}(\tilde{k} + \tilde{\kappa}^*) \\
& - \overline{\delta\psi}^{\mathrm{T}}(\tilde{e}_1 + \tilde{\gamma}^*)]F - [(\overline{\delta\psi}')^{\mathrm{T}} - \overline{\delta\psi}^{\mathrm{T}}(\tilde{k} + \tilde{\kappa}^*)]M + \overline{\delta q}^{\mathrm{T}}f_a^* + \overline{\delta\psi}^{\mathrm{T}}m_a^* \\
& + \overline{\delta P}^{\mathrm{T}}[-C_b^{\mathrm{T}}C_w^{\mathrm{T}}V^* + v + \tilde{\omega}(r + u)] - \dot{\overline{\delta P}}^{\mathrm{T}}u \\
& + \overline{\delta H}^{\mathrm{T}}[(\Delta + \tfrac{1}{2}\tilde{\theta} + \tfrac{1}{4}\theta\theta^{\mathrm{T}})C_b^{\mathrm{T}}(-\Omega^* + C_w C_b\omega)] \\
& - \dot{\overline{\delta H}}^{\mathrm{T}}\theta - \overline{\delta F}^{\mathrm{T}}[-C_b^{\mathrm{T}}C_w^{\mathrm{T}}(\gamma^* + e_1) + C_b^{\mathrm{T}}e_1] + (\overline{\delta F}')^{\mathrm{T}}u \\
& - \overline{\delta M}^{\mathrm{T}}[-(\Delta + \tfrac{1}{2}\tilde{\theta} + \tfrac{1}{4}\theta\theta^{\mathrm{T}})C_b^{\mathrm{T}}\kappa^*] + (\overline{\delta M}')^{\mathrm{T}}\theta \\
& + \overline{\delta\lambda}^{\mathrm{T}}[[A]^{-1}(\{\lambda\} - \{c\}\bar{\Gamma}^*)] - \dot{\overline{\delta\lambda}}^{\mathrm{T}}\{\lambda\} \Big\} \mathrm{d}x\, \mathrm{d}t \\
= & \int_0^\ell (\overline{\delta q}^{\mathrm{T}}\hat{P} + \overline{\delta\psi}^{\mathrm{T}}\hat{H} - \overline{\delta P}^{\mathrm{T}}\hat{u} - \overline{\delta H}^{\mathrm{T}}\hat{\theta} - \overline{\delta\lambda}^{\mathrm{T}}\{\hat{\lambda}\})|_{t_1}^{t_2}\, \mathrm{d}x \\
& - \int_{t_1}^{t_2} (\overline{\delta q}^{\mathrm{T}}\hat{F} + \overline{\delta\psi}^{\mathrm{T}}\hat{M} - \overline{\delta F}^{\mathrm{T}}\hat{u} - \overline{\delta M}^{\mathrm{T}}\hat{\theta})|_0^\ell\, \mathrm{d}t,
\end{aligned} \tag{20}
$$

where new Lagrange multipliers have been added to include the above constraints in the variational statement.

Note the constitutive equations and aerodynamic force equations are not applied as constraints because the expressions for the strain variables, velocity variables and the aerodynamic forces are written out explicitly using the constitutive equations and aerodynamic model so as to reduce the number of variables. In the above variational statement ( )* denotes the expressions for the variables using the equations presented earlier.

The weak Hamilton's principle can now be used to generate time-marching equations using space–time finite elements. To do so, the beam is discretized into n elements spatially and one element in time. Due to the weakest form of the variational statement, constant shape functions are used for the variables, and linear/bilinear shape functions are used for the test functions (Atilgan *et al.* 1996):

$$
\begin{array}{ll}
\delta u = \delta u_i(1 - \xi)(1 - \tau) + \delta u_j\xi(1 - \tau) + \delta u_k\xi\tau + \delta u_l(1 - \xi)\tau, & u = u_i, \\[4pt]
\overline{\delta\psi} = \overline{\delta\psi}_i(1 - \xi)(1 - \tau) + \overline{\delta\psi}_j\xi(1 - \tau) + \overline{\delta\psi}_k\xi\tau + \overline{\delta\psi}_l(1 - \xi)\tau, & \theta = \theta_i, \\[4pt]
\overline{\delta F} = \overline{\delta F}_i(1 - \xi) + \overline{\delta F}_j\xi, & F = F_i, \\[4pt]
\overline{\delta M} = \overline{\delta M}_i(1 - \xi) + \overline{\delta M}_j\xi, & M = M_i, \\[4pt]
\overline{\delta P} = \overline{\delta P}_i(1 - \tau) + \overline{\delta P}_j\tau, & P = P_i,
\end{array}
$$

$$\overline{\delta H} = \overline{\delta H_i}(1 - \tau) + \overline{\delta H_j}\tau, \qquad\qquad\qquad\qquad H = H_i,$$

$$\overline{\delta \lambda} = \overline{\delta \lambda_i}(1 - \tau) + \overline{\delta \lambda_j}\tau, \qquad\qquad\qquad\qquad \{\lambda\} = \{\lambda_i\}, \quad (21)$$

where τ and ξ are dimensionless elemental temporal and spatial co-ordinates, respectively.

Substituting the shape functions in Hamilton's principle one obtains a set of nonlinear algebraic equations which leads to a nonlinear implicit time-marching scheme. The equations for time-marching can be written as

$$- (P_f - P_i) - \Delta t \tilde{\Omega}_m^* P_m + \Delta t(F_r - F_l) + \Delta \ell \Delta t(\tilde{k} + \tilde{\kappa}^*)_m F_m + \Delta t \Delta \ell f_{am}^* = 0,$$

$$- (H_f - H_i) - \Delta t \tilde{\Omega}_m^* H_m - \Delta t \tilde{V}_m^* P_m + \Delta t(M_r - M_l) + \Delta \ell \Delta t(\tilde{k} + \tilde{\kappa}^*)_m M_m$$
$$+ \Delta \ell \Delta t(\tilde{e}_1 + \tilde{\gamma}^*)_m F_m + \Delta t \Delta \ell m_{am}^* = 0,$$

$$(u_f - u_i) + \Delta t \left[- C_b^T C_w^T V^* + v + \tilde{\omega}(r + u) \right]_m = 0,$$

$$(\theta_f - \theta_i) + \Delta t [(\Delta + \tfrac{1}{2}\tilde{\theta} + \tfrac{1}{4}\theta\theta^T) C_b^T(-\Omega^* + C_w C_b \omega)]_m = 0,$$

$$\frac{\Delta \ell}{2} [C_b^T C_w^T(\gamma^* + e_1) - C_b^T e_1]_m^j + \frac{\Delta \ell}{2} [C_b^T C_w^T(\gamma^* + e_1) - C_b^T e_1]_m^{j+1} - (u_m^{j+1} - u_m^j) = 0,$$

$$\frac{\Delta \ell}{2} [(\Delta + \tfrac{1}{2}\tilde{\theta} + \tfrac{1}{4}\theta\theta^T) C_b^T \kappa^*]_m^j + \frac{\Delta \ell}{2} [(\Delta + \tfrac{1}{2}\tilde{\theta} + \tfrac{1}{4}\theta\theta^T) C_b^T \kappa^*]_m^{j+1} - (\theta_m^{j+1} - \theta_m^j) = 0,$$

$$\Delta t [[A]^{-1}(\{\lambda\} - \{c\}\bar{\Gamma}^*)]_m + (\{\lambda\}_f - \{\lambda\}_i) = 0, \qquad (22)$$

where subscripts l and r are used to denote the left and right nodal forces, respectively, and subscripts i and f are used to denote the initial and final values of elemental displacements, element momenta and element inflow variables. Subscript m denotes the elemental (or interior) value for force and the value between the initial and final time for the displacement, momentum and inflow variables. The $(\ )_m$ values are the average of the $(\ )_l$ and $(\ )_r$ values or the average of the $(\ )_i$ and $(\ )_f$ values, as appropriate. Where necessary, the superscript denotes the element number.

Now knowing the initial displacements, momenta and inflow, one can calculate the displacements, momenta and inflow variables at the end of the time step along with the force in the interior. At each time step a set of nonlinear equations has to be solved iteratively to obtain the solution.

Note the above development of the aeroelastic model does not explicitly present the aerodynamic stall model. The stall model changes the aerodynamic loads model to incorporate the reduction in aerodynamic forces due to stall. The stall corrected expressions for the generalized aerodynamic loads and the circulation are,

$$L_{T_n} = L_n + \rho u_T \Gamma_n, \qquad \Gamma_T = \Gamma + \Gamma_\ell, \qquad (23)$$

where u_T is the total flow speed relative to airfoil, and the Γ_n are corrections in circulation due to stall corresponding to the various generalized loads. Γ_T denotes the corrected total circulation on the airfoil and Γ_ℓ represents the circulation correction corresponding to the total lift on the airfoil.

The inflow equations are also affected due to the change in the circulation caused by stall. The new inflow equations become

$$[A]\{\dot{\lambda}\} + \{\lambda\} = \{c\}(\bar{\Gamma} + \bar{\Gamma}_\ell). \qquad (24)$$

In the present simulations, a static stall model is used which models the reduction in the airfoil circulation based on the states at any given time as

$$\Gamma_n = - b u_T \Delta c_n, \qquad (25)$$

where Δc_n is the Glauert coefficient of correction in the lift coefficients. The stall-corrected airloads are inserted into the variational statement to complete the aeroelastic model including stall effects.

An ONERA-like stall model can also be modeled by including the dynamic stall equations. These equations would then be added as constraint equations to the complete variational principle in a way similar to the addition of the inflow equations. The results presented in this paper are based on a static stall model.

4. RESULTS

The primary aim of this paper is to present results pertaining to the nonlinear aeroelastic behavior of a high-aspect-ratio wing which may be used in high-altitude, long-endurance (HALE) aircraft. The behavior of a high-aspect-ratio wing is quite different from that of the low- or medium-aspect ratio wings designed for fighter or commercial aircraft, especially the nonlinear characteristics. Table 1 gives the structural and planform data for the wing model under investigation. The model was constructed by modifying Daedalus human-powered aircraft data and is representative of wings used in HALE aircraft. The stall data for the airfoil section is presented as a lift versus angle of attack plot in Figure 1.

There are various kinds of analyses possible to investigate the overall aeroelastic behavior of the wing under consideration. Firstly, one can do a linear eigenvalue analysis, which would predict the stability characteristics of the unloaded, undeformed wing. Secondly, one could trim the aircraft or apply representative static loads on the wing and calculate the nonlinear equilibrium position. The aeroelastic model can then be linearized about the nonlinear steady state to obtain a linearized eigenvalue problem. This eigenvalue analysis gives a more realistic prediction of the stability of the wing. In many cases such a linearized stability analysis cannot predict the response of the wing to large disturbances, nor can it predict whether the nonlinearities limit the magnitude of instability. Thus, the final option available to analyze the response of a wing is via time-marching. Such an analysis gives the actual response as a function of time and thus an indication of the complete behavior of the system.

Flutter speed is a linear concept, i.e., it gives the speed at which small disturbances grow. The linear as well as nonlinear flutter speed for this model has been calculated and

TABLE 1
Model data

| Wing	
Half-span	16 m
Chord	1 m
Mass per unit length	0·75 kg/m
Moment of inertia (50% chord)	0·1 kg m
Span-wise elastic axis	50% chord
Center of gravity	50% chord
Bending rigidity	2×10^4 N m^2
Torsional rigidity	1×10^4 N m^2
Bending rigidity (chordwise)	4×10^6 N m^2
Flight condition	
Altitude	20 km
Density of air	0·0889 kg/m^3
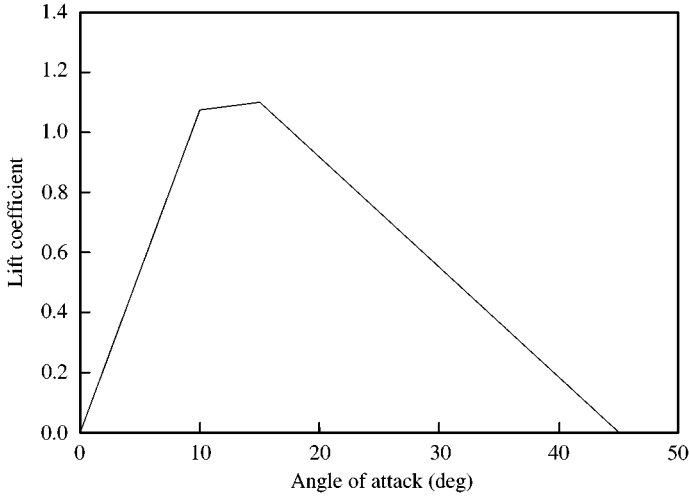
Figure 1. Plot showing the lift coefficient as a function of angle of attack.

presented in Patil *et al.* (1999). *Linear flutter speed* refers to the classical flutter speed calculated using a linear model or by linearizing a nonlinear model about a zero steady state. *Nonlinear flutter speed* refers to flutter speed calculated by linearizing a nonlinear model about a nonlinear steady state, i.e., a linear dynamic perturbation about a nonlinear static equilibrium state. The aim of the present work is to present results obtained by time-marching the equations of motion. These results give an overall perspective of the nonlinear aeroelastic response of high-aspect-ratio wings.

For reference, the linear flutter speed and frequency are 32·21 m/s and 22·61 rad/s, respectively, for the chosen parameters. Results are first presented for post-flutter behavior about the zero steady state. Then the aeroelastic response is analyzed by focusing on the changes in structural properties with wing deformation. These results are followed by LCO results for speeds below the linear flutter speed and finally a note on the existence and overall behavior of LCOs in high-aspect-ratio wings.

4.1. POST-FLUTTER BEHAVIOR

The effect of nonlinearities on the post-flutter behavior are considered in this section. An initial small disturbance of the order of 0·01 m tip vertical displacement is applied to excite the flutter mode for a flight speed of 35 m/s (slightly above the linear flutter speed). The time history of the tip displacement, tip twist and total energy of the wing are plotted in Figure 2. For such small disturbances the wing is initially in the linear regime and thus once the flutter mode is excited the amplitude of oscillations initially grow exponentially. At around 10 s the oscillations seem to settle into a limited amplitude oscillation. This is expected because of the stall characteristics of the airfoil. At higher angles of attack the airfoil stalls and is unable to extract additional energy from the flow and thus the amplitude vibration does not grow.

However, what seems like a converged LCO is not stable, and the oscillations undergo an unexpected change in the motion. This phenomenon is initiated by a drastic jump in the tip displacement. Instead of oscillating about tip displacement values near zero, the oscillations are shifted. This jump is also accompanied by an increase in the amplitude of oscillations. The oscillations are of the order of 1·5 ± 1·0 m. The response is quite chaotic due to the
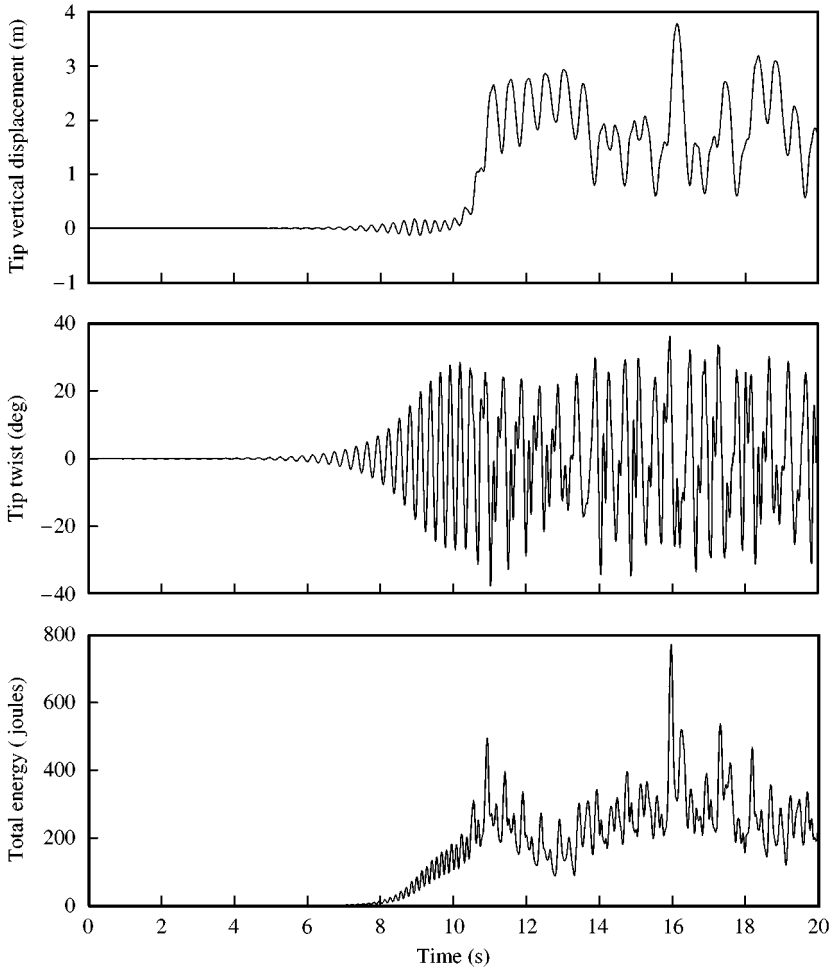
Figure 2. Time history showing LCO above flutter speed (speed of 35 m/s) for HALE wing.

strong geometric nonlinearities associated with large oscillations (tip displacements varies between 0·5 and 2·5 m). The geometric nonlinearities due to tip displacement and its effect on aeroelastic response is explained in detail in the following section.

An alternative way to investigate nonlinear motion is via a phase-plane graph. Such graphs plot two variable against each other for various times. Phase-plane plots give an indication as to the kind of motion, periodic or chaotic, and other characteristics of a nonlinear problem. Figure 3 shows the phase-plane plots of the oscillation at a speed of 35 m/s. The plots show the history of motion after limited amplitude oscillations are reached. It is observed that the oscillations are aperiodic and quite chaotic.

4.2. Structural Nonlinearity in High-Aspect-Ratio Wings

Before presenting results concerning LCO at other speeds, it is helpful to characterize the structural geometric nonlinearities arising from the large deformation of the wing. This nonlinearity is primarily responsible for the jump in the tip displacement in the results presented in the earlier section. This nonlinearity is also very important in understanding the results to follow.
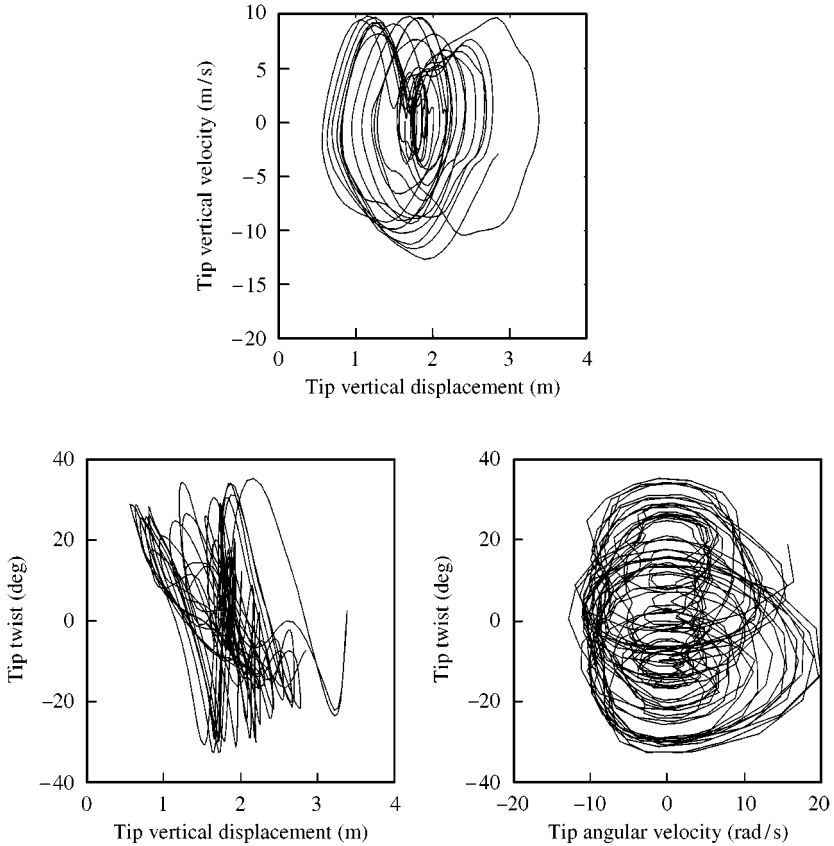
Figure 3. Various phase-plane plots at speed of 35 m/s.

A long slender wing like the one considered in this paper is highly flexible. Such wings undergo large deformations for relatively low loadings as compared to low-aspect ratio wings. Also the natural frequencies of high-aspect-ratio wings are quite low. From the simple formulae for natural frequencies of a beam-rod it is clear that torsional frequencies are inversely proportional to the length while the bending frequencies are inversely proportional to the square of the length. Thus, we have the bending frequencies decreasing at a higher rate than the torsional frequencies as the wing span increases. And thus the frequency distribution of a long slender wing is quite different from that of low-aspect-ratio wings. High-aspect-ratio wings have a very low flapping frequency (flat-wise bending), while the edge-wise bending frequency decreases to be of the order of the torsional frequency.

Now, it is known that when the wing is bent (flat-wise) this leads to a nonlinear coupling between torsion and edge-wise bending (Hodges & Dowell 1974). Since high-aspect-ratio wings undergo large flat-wise bending deformation under the action of lift there is a strong nonlinear coupling between edge-wise bending and torsion. To appreciate the magnitude of the nonlinear effect of deformation, the structural and aeroelastic characteristics of the wing are investigated by linearizing the problem about a nonlinear statically deformed state.

There are various ways of obtaining a deformed state. In the results presented, a static force is applied to the wing tip leading to static deformation of the wing (in flat-wise bending). Another way of obtaining a static wing deflection is via a trim angle of attack.

Such an analysis leads to a complex effect on the flutter speed (Patil *et al.* 1999). This behavior is attributed to the fact that the static deflection of the wing due to a trim angle of attack changes with speed while on the other hand, the flutter speed is itself a function of the static displacement. The results are best understood by applying tip deflections which are independent of the speed and thereby leading to a simpler relation between the deformation and the flutter.

In the present work, a specified static force is applied at the tip to create a static deformed state. The problem is linearized about this deformed state to obtain a linear model for eigenvalue analysis. Figure 4 shows the changes in natural frequencies for a range of static tip displacements. The tip displacements are of the order expected under nominal aerodynamic loads due to a trim angle of attack. One can see that there is a strong coupling between the edge-wise bending and torsional frequencies due to static flat-wise bending displacements. Such coupling leads to a separation of the two frequencies. In the present case, we observe a decrease in the coupled torsional/edge-wise frequency which was originally purely torsional. This important nonlinear behavior has been presented by Minguet & Dugundji (1990) who analytically as well as experimentally showed the changes in the torsion and edge-wise bending modes for coupled and uncoupled composite strips [see also Dowell *et al.* (1977)].

Figure 5 shows the changes in nonlinear flutter speed and flutter frequency with static wing deformation. There is a drastic decrease in the flutter speed with static tip displacement. This is due to a decrease in the frequency of the torsional/edge-wise bending mode, as discussed above. As explained in Patil *et al.* (1999), the decrease in the torsional/edge-wise bending frequency more readily leads to coalescence with the second flat-wise bending mode, and thus flutter at lower velocities. For larger static wing deformation the frequency of the torsional/edge-wise bending mode continues to decrease and thus the flutter frequency decreases. For a static tip displacement of about 2 m the torsional/edge-wise bending frequency is approximately equal to the second flat-wise bending mode and thus the flutter speed is relatively unchanged in this range of static tip displacement. For even higher deformations there is a further decrease in torsional/edge-wise bending frequency putting the mode closer to the first-bending mode and there is a further decrease in the flutter speed. Thus, the flutter characteristics of a curved wing are very different from those of a straight wing due to the structural geometric nonlinearities. It is seen that the flutter instability is greatly influenced by a static tip displacement, which is an important fact to be considered while analyzing the nonlinear aeroelastic results.

For a given flow speed one can plot the damping of the unstable aeroelastic mode with respect to static tip displacement. Damping is found in the same way that the flutter speed is calculated, i.e., the problem is linearized at a given static tip displacement and a given speed and the eigenvalues of the linearized problem are calculated to give the frequency and damping of the various modes. Figure 6 shows the changes in frequency and damping of the flutter mode with tip displacement for a flow speed of 35 m/s. The sign convention chosen is such that positive damping signifies unstable motion.

As expected for a speed of 35 m/s, the damping is positive (unstable) even for no deformation. But the damping (and thus the instability) increases with increase in deformation. The positive slope of damping with tip displacement indicates that the instability of the system becomes more pronounced with increasing static tip displacement. This is a very important phenomenon and could be the primary cause of most of the nonlinear aeroelastic behavior presented here. It is theorized here that the jump in the tip displacement in the LCO at 35 m/s is due to an attraction of the system to a more unstable state. As seen in the damping plot, the instability is maximum at a tip displacement of around 1–1·5 m and thus the wing LCO jumps to an oscillation with a mean of around 1·5 m.
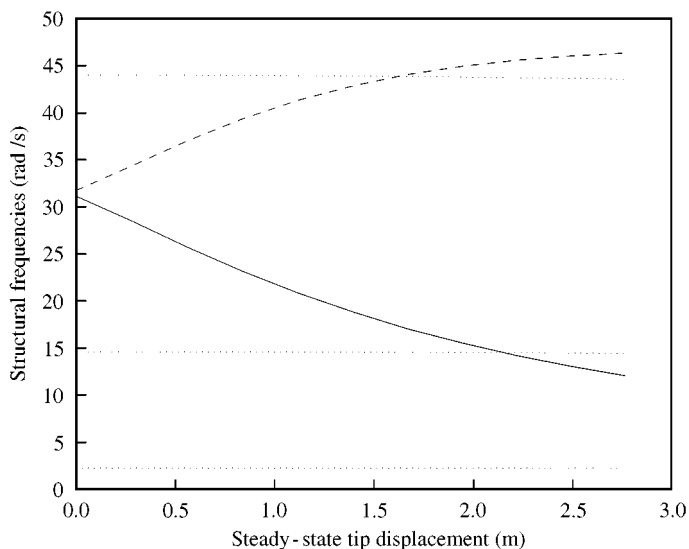
Figure 4. Variation of structural frequencies with tip displacement: ——, torsion/edge-wise bending; - -, edge-wise bending/torsion; ·····, flat-wise bending.
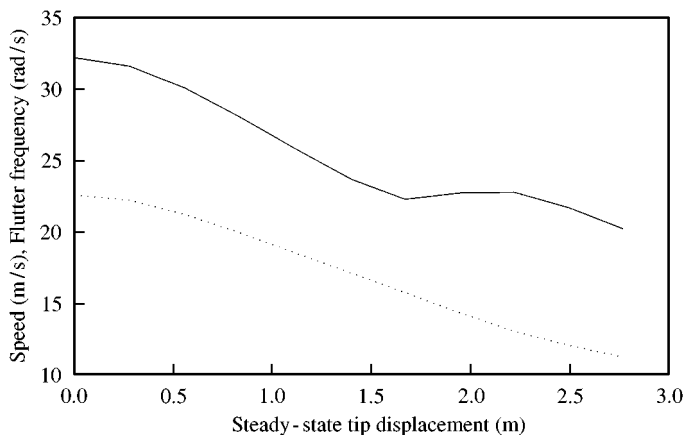

Figure 5. Variation of flutter speed (——) and flutter frequency (·····) with tip displacement.

The system instability becomes stronger by having a mean tip displacement and thus there is a greater flow of energy from the surrounding air into the wing. For the system to go into the stronger instability, a mean tip displacement should be maintained. The system needs to somehow dynamically maintain the mean deformation shape by appropriately providing a mean force. If such a force could be easily provided then it would mean an easy transition into a state with a stronger instability.

4.3. PRE-FLUTTER LCO

As shown in Figure 5, the flutter speed for a wing displaced from the no loads equilibrium straight configuration is much lower than the linear flutter speed (corresponding to zero
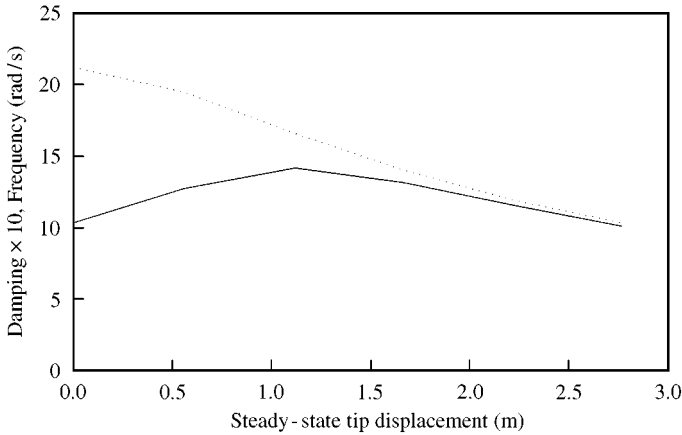
Figure 6. Variation of damping (——) and frequency ($\cdots$) with tip displacement at flight speed of 35 m/s.

static tip displacement). It is thus obvious that if the wing is statically deformed then it could encounter an instability at lower speeds. But an interesting case is when the wing with zero-deflection equilibrium state is given an initial deflection into the unstable regime, for example a gust-induced deflection. Figure 7 shows the time history of a wing at 30 m/s given an initial disturbance of 2·0 m. The speed of 30 m/s is lower than the linear flutter speed, but higher than the nonlinear (linearized) flutter speed for a wing which is statically displaced to 2·0 m at the tip.

The deflected shape is very close to the first-bending mode. It is clear that in the deflected position, there is no static load to support the deflected position (since it is just an initial deflection). Thus, the wing moves to regain its zero-deflection equilibrium position and one finds a decrease in the tip displacement. It is seen that as the first-bending mode decays, the unstable flutter mode (which exists for a deflected state) is excited. This is seen in the exponential increase in the tip twist and the high-frequency component of tip dispacement. Furthermore, before the wing enters the stable region (for tip displacement of around 0·5 m as is shown later) it gains enough energy to jump to deflected mode with tip deflection of around 1·5 m. At the deflected state the wing is unstable and continues oscillating. As to why the wing jumps to this "non-equilibrium" state is not entirely clear but can possibly be explained by the changes in flutter mode damping with tip displacement.

Figure 8 shows the damping versus tip-displacement plot for the wing at 30 m/s. Again, the plot is obtained by first applying a static tip force to model a deflected wing and then conducting an eigenvalue analysis of the linearized aeroelastic model. As expected, the damping is negative (stable) for the undeflected position, but the damping quickly increases and reaches zero for a tip displacement of around 0·5 m. At higher tip displacements, the damping is positive and the system is unstable. Thus, while the system tries to come back to a zero-deflection, stable, equilibrium-state, it passes through a dynamically unstable state, and thus the system dynamically absorbs energy. If the system absorbs more than a critical amount of energy before it reaches the zero steady state, it then jumps to a high-energy unstable state (oscillating about a non-equilibrium deformed state) and dynamically provides the forces required to maintain a mean deformed state (required to stay unstable). The positive slope of the damping with respect to tip displacement is an indication to the system of higher instability at higher displacements.

The LCO at 30 m/s though quite complex is still very different from the LCO at 35 m/s. Figure 9 shows phase-plane plots of the wing after it reached LCO. It is seen that the motion
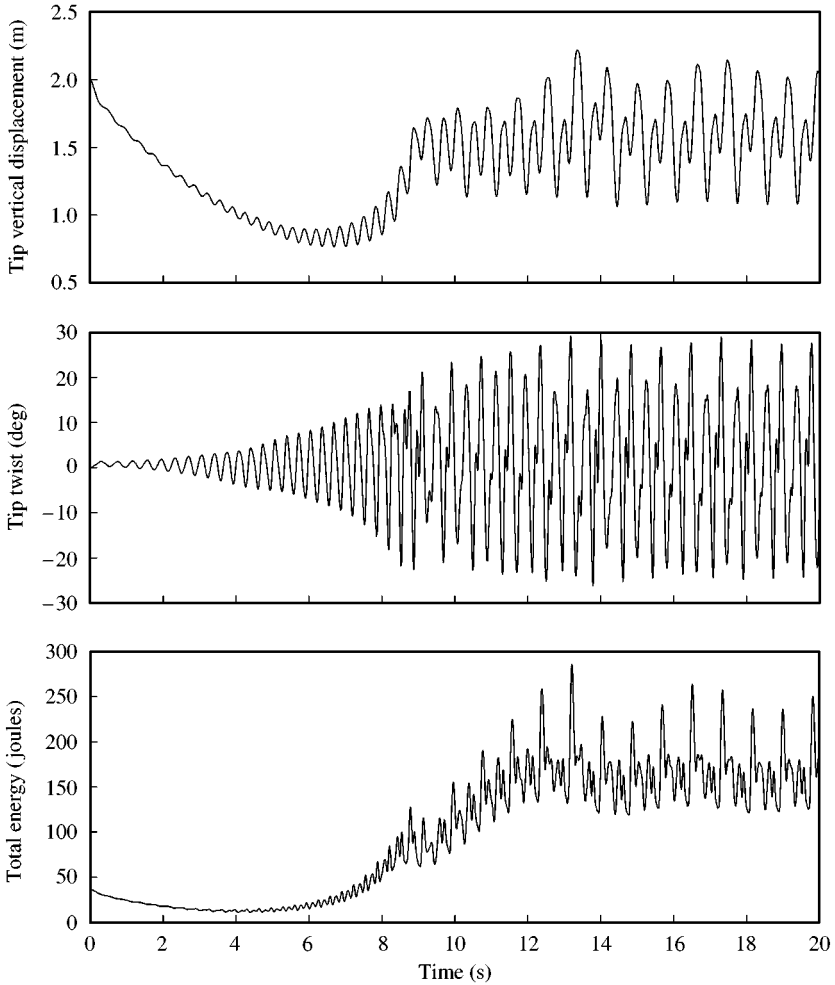
Figure 7. Time history showing LCO below flutter speed (speed of 30 m/s) for HALE wing.

is complex but periodic. The motion is a combination of several subharmonics. Subharmonics lead to an increase in period for the system to return to a given position, and are seen in the phase-plane plots as loops. The LCO is complex but periodic, as opposed to LCOs at 35 m/s which seem chaotic.

4.4. LCO DEPENDENCE ON DISTURBANCE

For the present wing with a linear flutter speed of 32·21 m/s it is clear that an infinitesimally small disturbance at a speed of 30 m/s would lead to a stable return to equilibrium state. Such an inference can be drawn from the stable eigenvalues which imply a stable response to small disturbances. On the other hand, it is seen that, if the wing is given a sufficiently large deformation, then it might not only have unstable behavior while it is away from the stable equilibrium, but the wing response might never return near enough to the stable equilibrium position for convergence, but instead jump to an unstable state. Thus, to excite the flutter modes below the flutter speed a finite disturbance is required.
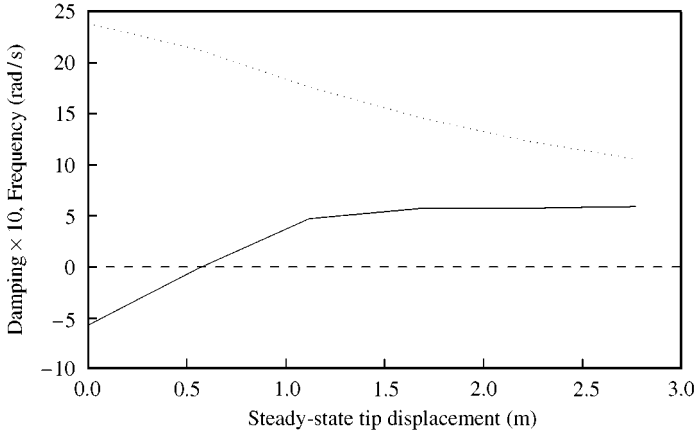
Figure 8. Variation of damping (——) and frequency (·····) with tip displacement at flight speed of 30 m/s.
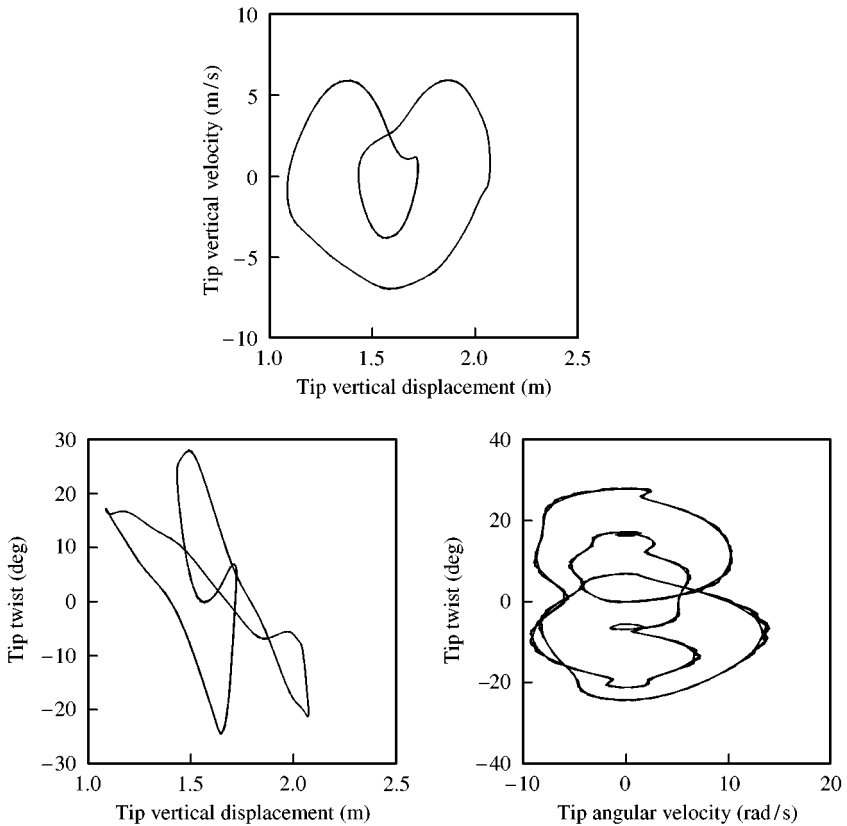
Figure 9. Various phase-plane plots for speed of 30 m/s (initial disturbance = 2 m).

The wing can thus become unstable even for a nominally stable static equilibrium if a sufficiently large disturbance is provided. Figure 10 presents the system response at 30 m/s given various initial tip disturbances. It is observed that the wing is attracted to a LCO for tip disturbances of 2 and 4 m, whereas, the wing returns to the stable equilibrium for
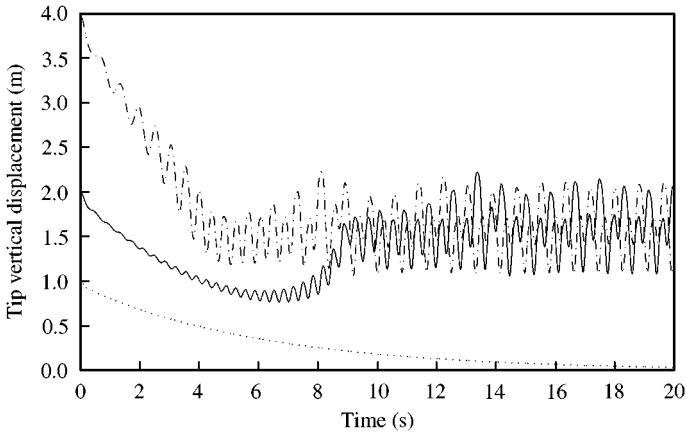
Figure 10. Response of the wing at 30 m/s for various initial tip disturbances: ····, 1 m; ——, 2 m; ·—·—, 4 m.
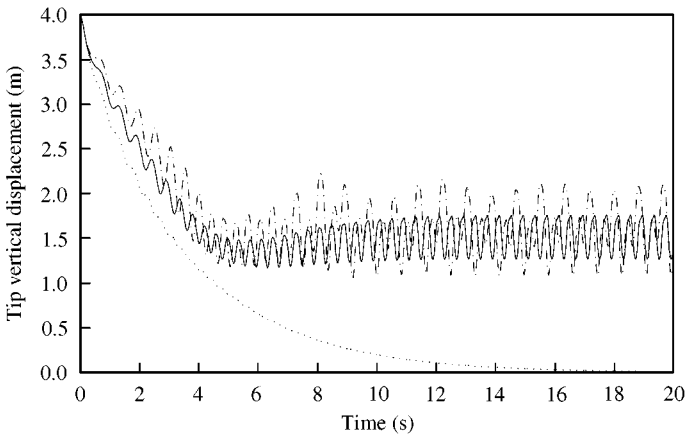
Figure 11. Response of the wing for an initial disturbance of 4 m at various velocities: ·····, 25 m/s; ——, 28 m/s; ·—·—, 30 m/s.

a disturbance of 1 m. The later behavior is because, as the deflected mode (similar to first-bending mode) decays, the excited flutter mode does not gain energy enough to jump to unstable motions with higher energy. As the first-bending mode decays, the wing enters the stable region and then returns to the zero-deflection stable equilibrium. Thus, a critical magnitude of disturbance is required to excite a LCO at a given speed. On the other hand, initial deflections of both 2 and 4 m lead to almost identical LCO, with similar mode, magnitude and frequency content. Thus, it can be inferred that the LCO does not change with change in disturbance.

Figure 11 presents the system response at various speeds given a constant initial disturbance amplitude of 4 m. It is seen that at 28 and 31 m/s the system goes into a LCO, whereas at 25 m/s, the system is unable to accumulate enough energy to jump to an unstable state of oscillations. Thus, for a given disturbance a critical speed is required to excite the LCO. Above the critical speed, one observes different LCOs for various speed. The magnitude of the LCOs is higher for higher speeds and the mode shapes are different, thus indicating a change in LCOs with speed. The various kinds of LCOs are discussed in the next section.
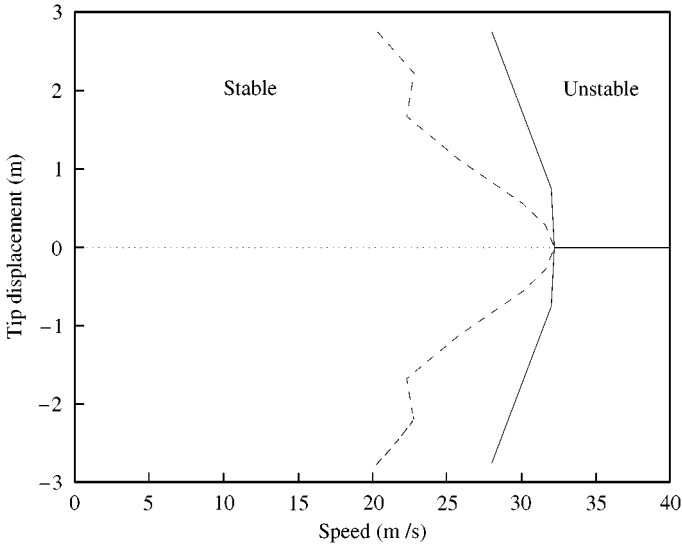
Figure 12. Plot of LCO boundary in the airspeed versus tip-displacement space: - - -, boundary of unstable equilibrium; ——, boundary of unstable disturbance about zero equilibrium.

The relation between the existence of LCO at various speeds and the level of disturbance is very important. For example, a given level of turbulence would excite a given level of disturbance and for that level of disturbance there is a critical speed required for LCO. This indicates that at velocities lower than the critical LCO speed, the wing would return to the stable equilibrium position. Thus, one can determine a LCO boundary which is a speed above which there is a possibility of LCO. Depending on the level of disturbance expected in flight, one would be able to predict a LCO boundary, i.e., the maximum flight speed possible without encountering LCO at the assumed level of disturbance.

Figure 12 shows the various flutter and LCO boundaries. The linear flutter is observed at 32·21 m/s, i.e., small disturbances about the undeformed equilibrium position would lead to decaying response for speeds below 32·21 m/s and divergent oscillations for speeds higher than 32·21 m/s. On the other hand, the LCO boundary denotes the magnitude of disturbance required for oscillations to diverge from the undeformed equilibrium solution. It is seen that for speeds below the linear flutter speed there is a critical level of disturbance required for divergent oscillations. Lastly, the nonlinear flutter curve denotes the static equilibrium positions (of a statically loaded wing) which are unstable for even small disturbances.

4.5. THE TRANSITION OF LCO BEHAVIOR WITH SPEED

From the previous sections it is observed that LCOs are possible at various speeds. The LCO type was drastically different for the pre- and post-flutter cases. In this section, the LCO behavior is investigated at various other speeds to investigate the types of LCOs possible. Phase-plane plots are obtained for aeroelastic simulations at speeds of 25, 28, 31 and 33 m/s, in addition to already presented simulations at 30 and 35 m/s. It is of primary interest to understand the types of LCO and how the LCO behavior changes with speed. Such analysis would lead to an answer as to why some LCOs are periodic while others are chaotic.

Here it is assumed, based on the results presented in the previous section, that a critical disturbance is required to induce LCO. However, past the critical disturbance the LCO

which is developed is relatively insensitive to the level of the disturbance. Thus, the required disturbance is provided for the wing to attain LCO at different speeds and then the LCOs are compared. At a flight speed of 25 m/s the wing does not go into a LCO even for large bending tip displacements. From the flutter versus tip displacement plot (Figure 5) it is seen that the lowest flutter speed is about 22 m/s. Thus, it is likely that LCOs exist at 25 m/s. An effective initial disturbance mode shape can be calculated by considering a snapshot of LCO at a higher speed (for example, a LCO snapshot at $V = 28$ m/s). Using such an initial condition the wing time history is calculated and it is seen that the wing is attracted to a LCO. Figure 13 shows the phase-plane plot of LCO at 25 m/s. The LCO seems to be almost sinusoidal. But the motion has a higher harmonic component obvious in the shape of the phase-plane plot (sinusoidal oscillations would lead to ellipsoid in any phase-plane). To investigate further the frequency content of the LCO one can obtain a frequency spectrum of the LCO. Figure 14 shows the frequency spectrum of the LCO at 25 m/s. As can be seen, there is a dominant frequency at around 16 rad/s. But there also exist second, third and higher super-harmonics at 32, 48 rad/s, etc.

A LCO is induced in the wing at speed of 28 m/s for a disturbance of 4 m at the tip. Figure 15 shows the phase-plane plot of the LCO. This phase-plane plot is a little more complex as compared to the phase-plane plot of LCO at 25 m/s. The looping of the phase-plane suggests that there is period doubling, i.e., the system returns to its original state after two periods. Such a period doubling is not uncommon in nonlinear systems and is due to the existence of subharmonics. Figure 16 shows the corresponding frequency spectrum. Here the phenomenon of period doubling is seen in the presence of a subharmonic peak at around 8 rad/s.

At flight speed of 31 m/s, there is further increase in the complexity of the LCO. Figure 17 shows the phase-plane plot at 31 m/s. Many more loops are observed. The LCO has a very large period. Figure 18 shows the corresponding frequency spectrum. In the frequency spectrum it is clear that the period is further tripled. It thus takes six periods to come back to the original state. At speeds close to or higher than the linear flutter speed the periodic pattern is lost altogether. Figure 19 shows the phase-plane plots at speed of 33 m/s which are aperiodic, i.e., the period is infinite. This is seen in the frequency spectrum (Figure 20) as a broadening of the spectrum.

If one looks at all the phase-plane plots, one can observe an increase in complexity of the LCO with speed. Period doubling occurs between 25 and 28 m/s; the complexity increases after 31 m/s and at around 32 m/s the response starts losing its periodicity (though it is still bounded). At 25 m/s there are only superharmonics to the dominant flutter/LCO frequency of around 16 rad/s, whereas at 28 m/s there is a subharmonic at half the frequency. Thus, the frequency spectrum changes from a $1, 2, 3, \ldots$, spectrum to a $\frac{1}{2}, 1, \frac{3}{2}, 2, \frac{5}{2}, 3, \ldots$, spectrum. At 31 m/s, the frequency spectrum undergoes a further period tripling. Thus, there are six subharmonics at 31 m/s and the response thus has a $\frac{1}{6}, \frac{2}{6}, \frac{3}{6}, \frac{4}{6}, \frac{5}{6}, 1, \frac{7}{6}, \ldots$, spectrum. The frequency content of the LCO further increases with speed, and thus a broadening of the frequency peaks is observed at 33 m/s. The initial frequency doubling followed by the broadening of the frequency spectrum is a tell-tale sign of chaotic behavior. Table 2 summarizes the results for LCO obtained on the HALE wing.

4.6. NUMERICAL CONVERGENCE

There is a need to comment on the accuracy of the solutions obtained in the present work since the solution technique is based on numerical calculations, and especially since those calculations are based on discretization of the continuous space. Firstly, it is necessary to look at the convergence properties of the solution. The present problem has been discretized
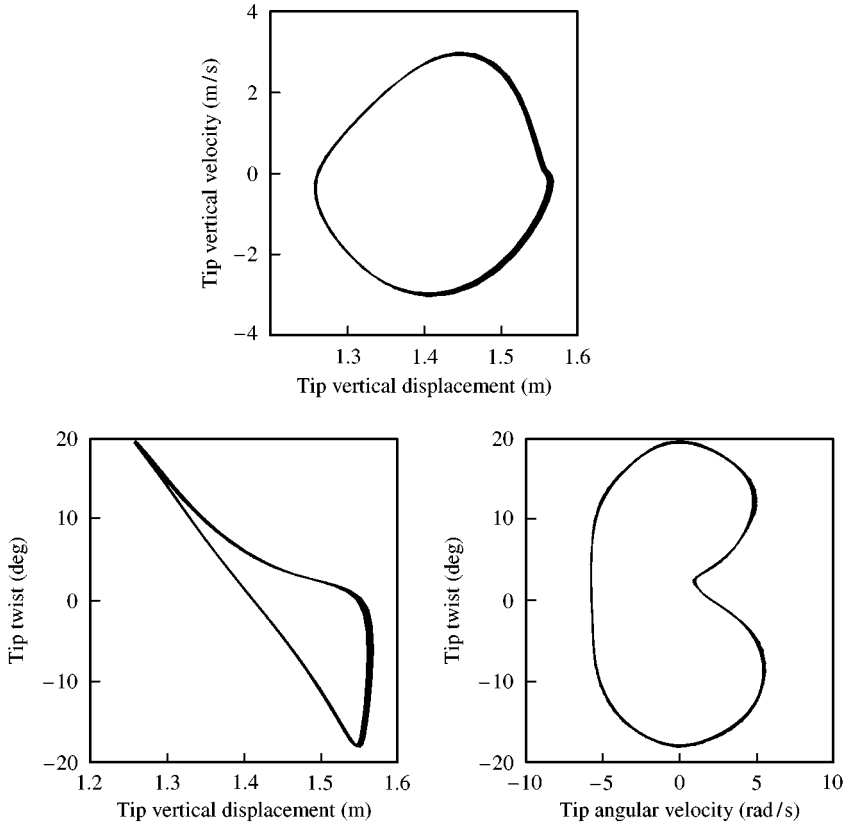
Figure 13. Various phase-plane plots for speed of 25 m/s (initial disturbance is a prior flutter condition).
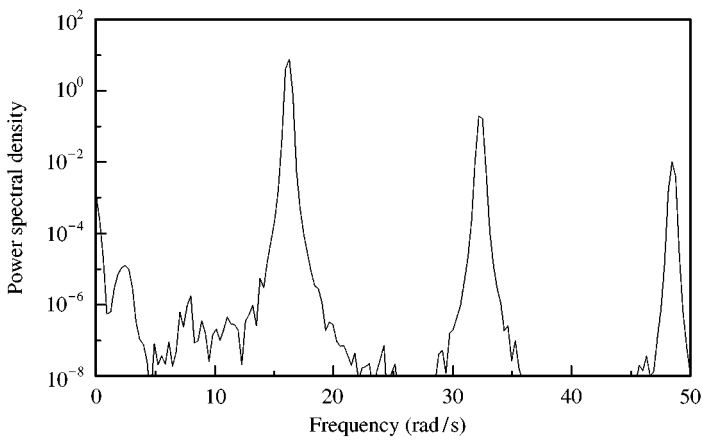

Figure 14. Power spectral density for speed of 25 m/s (initial disturbance is a prior flutter condition).
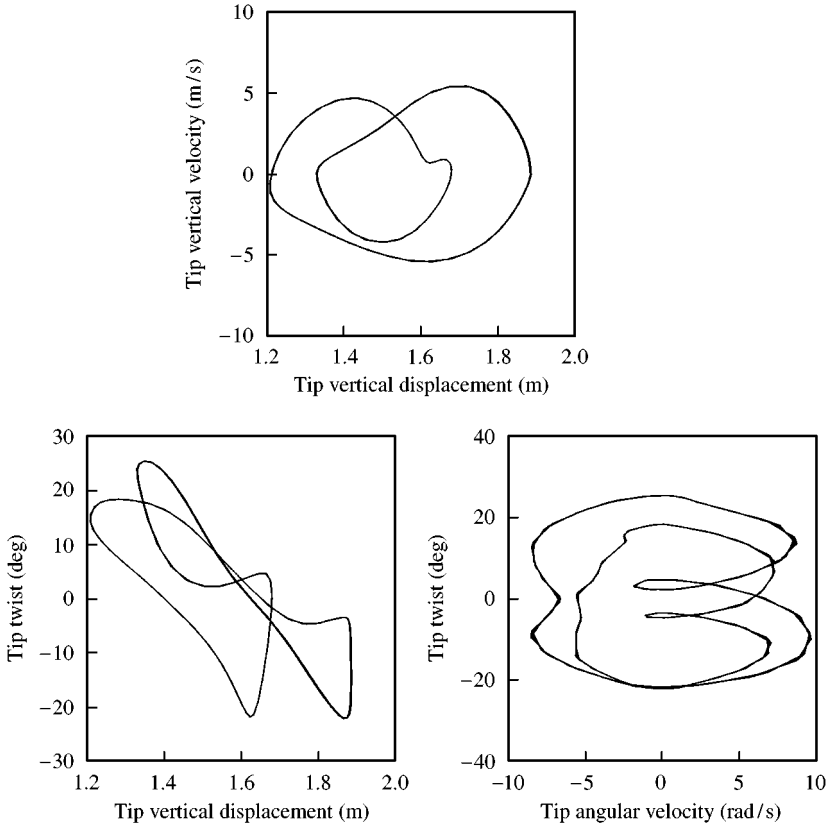
Figure 15. Various phase-plane plots for speed of 28 m/s (initial disturbance = 4 m).
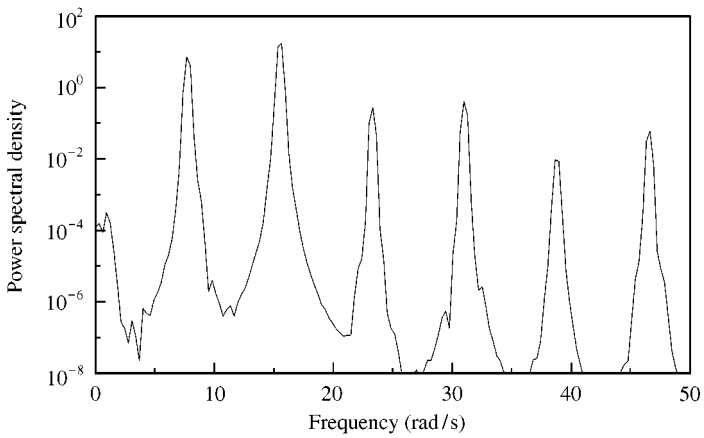
Figure 16. Power spectral density for speed of 28 m/s (initial disturbance = 4 m).
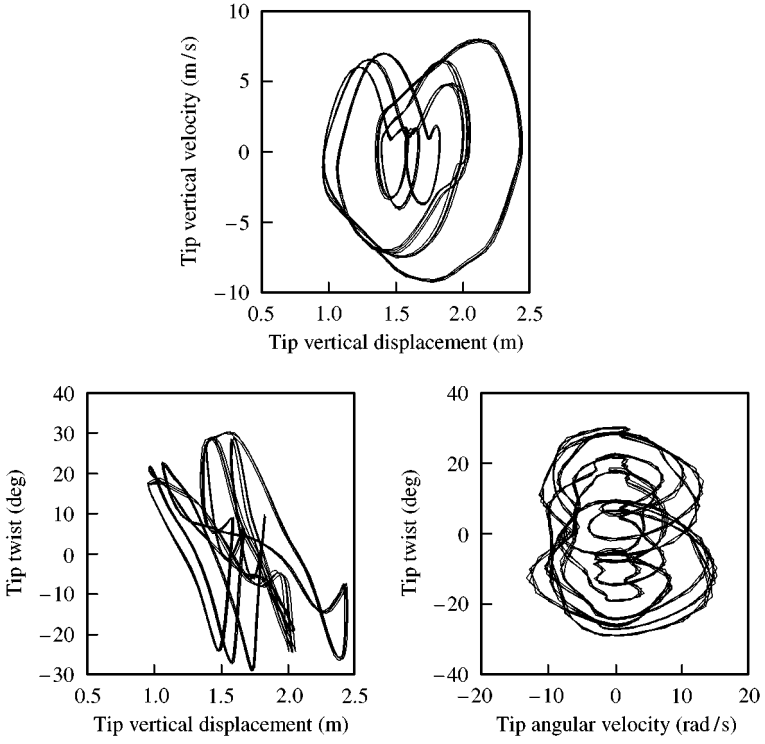
Figure 17. Various phase-plane plots for speed of 31 m/s (initial disturbance = 2 m).
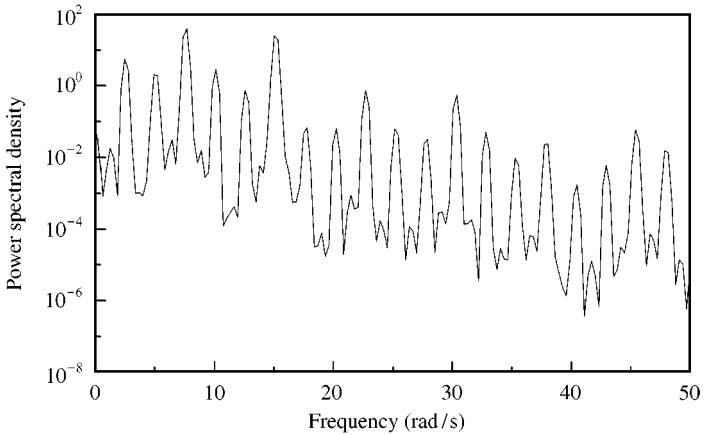
Figure 18. Power spectral density for speed of 31 m/s (initial disturbance = 2 m).
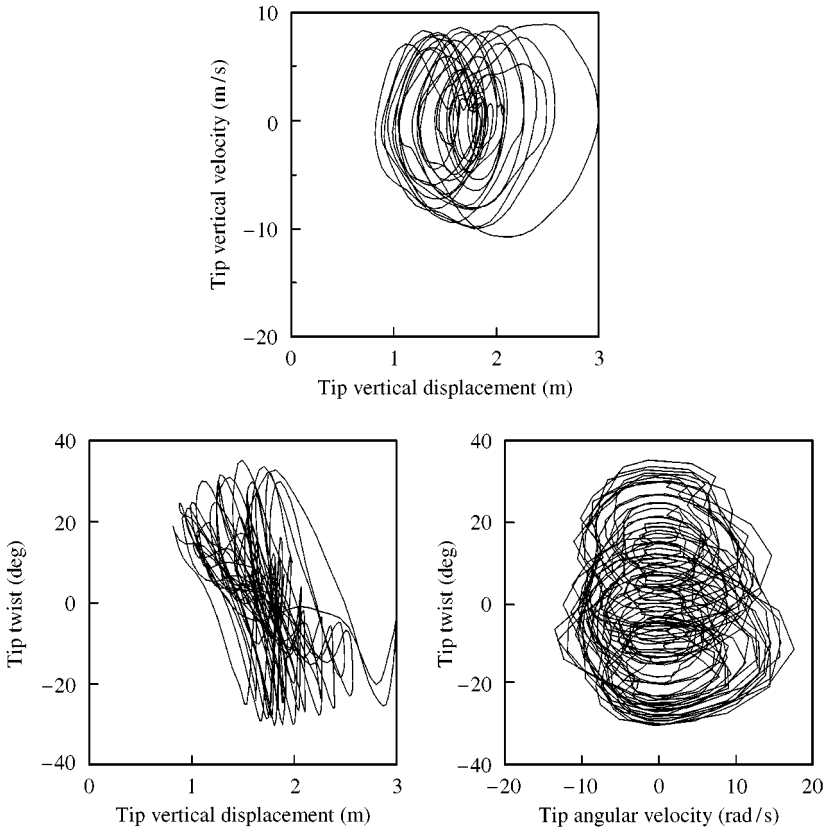
Figure 19. Various phase-plane plots for speed of 33 m/s (initial disturbance = 0·01 m).
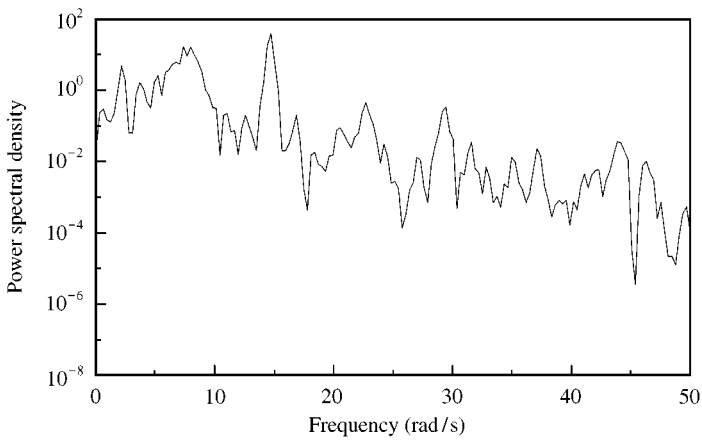
Figure 20. Power spectral density for speed of 33 m/s (initial disturbance = 0·01 m).

TABLE 2
Observed LCO chart for HALE wing

Initial disturbance	25 (m/s)	28 (m/s)	30 (m/s)	31 (m/s)	32 (m/s)	35 (m/s)
0·01 m	Stab.	Stab.	Stab.	Stab.	Stab.	LCO
1 m	Stab.	Stab.	Stab.	Stab.	LCO	LCO
2 m	Stab.	Stab.	LCO	LCO	LCO	LCO
4 m	Stab.	LCO	LCO	LCO	LCO	LCO
6 m	Stab.	LCO	LCO	LCO	LCO	LCO
Flutter	LCO	LCO	LCO	LCO	LCO	LCO
Type			Periodic		Chaotic	
Periodicity	$1, 2 \ldots$	$\frac{1}{2}, 1, \frac{3}{2}, 2, \ldots$		$\frac{1}{6}, \frac{2}{6}, \ldots$	—	

in space as well as time. The spatial discretization can be easily checked by comparing the natural frequencies of the discretized model with the natural frequencies calculated analytically for a prismatic beam. It is found that for the case of eight elements considered here the error in frequency of the dominant modes, viz., first torsion, first edge-wise bending as well as the first two flat-wise bending, is less than 1%.

As to the temporal discretization, it is firstly noted that the present time-marching scheme based on time-finite elements is second-order accurate. To compare the convergence of the simulations, the time histories are presented for various time steps. Figure 21 presents the simulation of a wing at 30 m/s given initial tip deflection of 2 m. It is seen that the simulation results are qualitatively the same for time step of 0·01, 0·005, and 0·002 s. Quantitatively, there is slight difference in the simulations, including small differences in the amplitude of oscillations and some periodicity error. The modeshape and type of LCO are the same. It can be safely said that the overall conclusions drawn from any of the plots would be exactly the same.

It is also essential here to look at a case in which the final oscillation is chaotic (aperiodic). Such is the case for post-flutter LCO. Figure 22 shows the wing simulation at 35 m/s given a small initial disturbance. Here it is seen that the system behavior is predicted quite accurately before the onset of chaotic LCO, after which the simulations for the different time steps are quite different. It should be noted though, that the wing is undergoing chaotic oscillations, and thus small differences grow drastically. But even though the details of the oscillations are quite different, the conclusions that can be drawn using any one of the plots are essentially the same, i.e., the wing response initially grows exponentially, later the wing jumps to a tip oscillation of around $1 \cdot 5 \pm 1 \cdot 0$ m.

5. CONCLUDING REMARKS

The phenomenon of a limit-cycle oscillation is numerically studied for a subsonic high-aspect-ratio wing. Due to large displacements and rotations, the results account for structural and aerodynamic nonlinearities through the use of a geometrically exact beam analysis and finite-state unsteady aerodynamics with stall. As expected, the results show that stall limits the amplitude of post-flutter unstable oscillations. On the other hand, a decrease in flutter speed is observed with wing deformation which can be attributed to structural geometrical nonlinearities. Even at speeds below the linear flutter speed, LCO can be observed if the stable steady state is disturbed by a finite-amplitude disturbance. A critical disturbance magnitude is required at a given speed and a critical speed is required
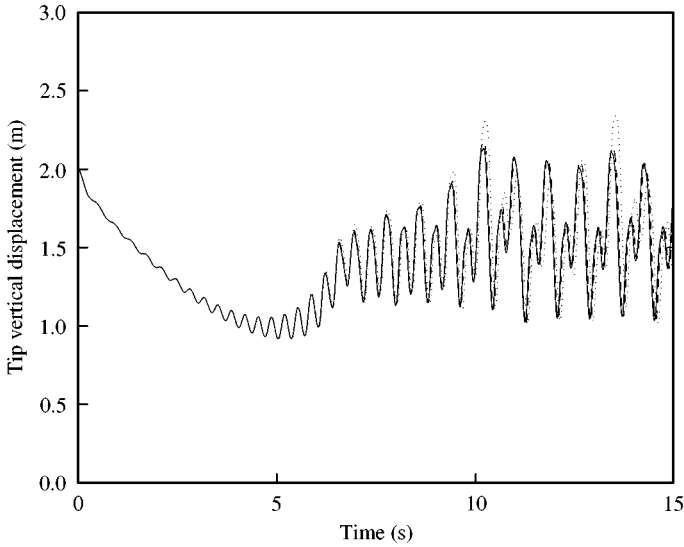
Figure 21. Numerical convergence: simulation of wing at a speed of 30 m/s given an initial disturbance of 2 m at the tip; $\cdots$, $\Delta t = 0 \cdot 01$ s; - - -, $\Delta t = 0 \cdot 005$ s; ——, $\Delta t = 0 \cdot 002$ s.
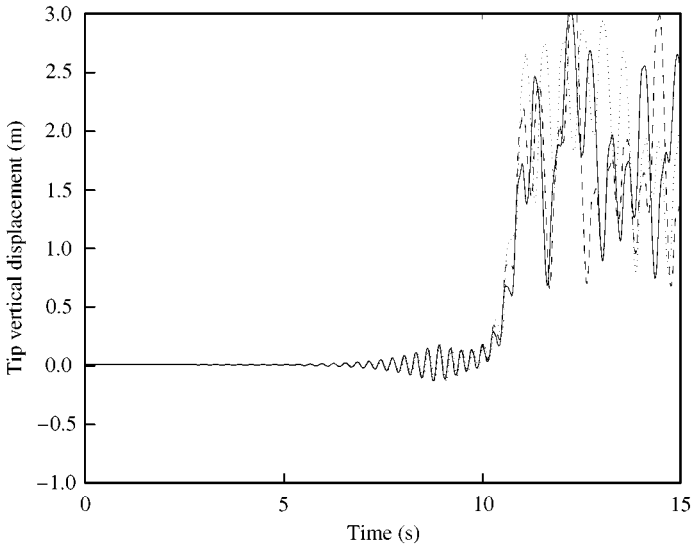
Figure 22. Numerical convergence: simulation of wing at a speed of 35 m/s given an initial disturbance of 0.01 m at the tip; $\cdots$, $\Delta t = 0 \cdot 01$ s; - - -, $\Delta t = 0 \cdot 005$ s; ——, $\Delta t = 0 \cdot 002$ s.

at a given disturbance magnitude to initiate LCO. Moreover, a loss of periodicity in the oscillations is observed for high speeds.

Such results give an indication of the nonlinear behavior expected of long, flexible wings and the need for a complete consistent nonlinear analysis. The change in flutter speed with respect to loaded or trimmed state is quite drastic. Linear analysis leads to over-prediction of the flutter speed and thus is quite dangerous. Even a static trimmed analysis may not be sufficient to completely understand the nonlinear aeroelastic phenomenon observed in long,

flexible wings. Complete nonlinear dynamic aeroelastic simulations are necessary, even during the preliminary design stage where catastrophic nonlinear phenomena can be most efficiently avoided.

ACKNOWLEDGEMENTS

REFERENCES

ATILGAN, A. R., HODGES, D. H., OZBEK, A. M. & ZHOU, W. 1996 Space-time mixed finite elements for rods. *Journal of Sound and Vibration* **192,** 731–739.

DOWELL, E. H., TRAYBAR, J. & HODGES, D. H. 1977 An experimental–theoretical correlation study of non-linear bending and torsion deformations of a cantilever beam. *Journal of Sound and Vibration* **50,** 533–544.

DUNN, P. & DUGUNDJI, J. 1992 Nonlinear stall flutter and divergence analysis of cantilevered graphite/epoxy wings. *AIAA Journal* **30,** 153–162.

GILLIATT, H. C., STRGANAC, T. W. & KURDILA, A. J. 1998 On the presence of internal resonances in aeroelastic systems. In *Proceedings of the 39th Structures, Structural Dynamics, and Materials Conference*, pp. 2045–2055, Long Beach, CA.

HODGES, D. H. 1990 A mixed variational formulation based on exact intrinsic equations for dynamics of moving beams. *International Journal of Solids and Structures* **26,** 1253–1273.

HODGES, D. H. & DOWELL, E. H. 1974 Nonlinear equations of motion for the elastic bending and torsion of twisted nonuniform rotor blades. Technical Report TN D-7818, NASA.

LIND, R., SNYDER, K. & BRENNER, M. 1998 Investigating transient and limit cycle behaviors of a nonlinear structure by wavelet transforms. In *Proceedings of the 39th Structures, Structural Dynamics, and Materials Conference*, pp. 942–952, Long Beach, CA.

MINGUET, P. & DUGUNDJI, J. 1990 Experiments and analysis for composite blades under large deflections. Part ii—dynamic behavior. *AIAA Journal* **28,** 1580–1588.

NAYFEH, A. H. & MOOK, D. T. 1979 *Nonlinear Oscillations*. New York: John Wiley and Sons.

O'NEIL, & T. STRGANAC, T. W. 1996 Nonlinear aeroelastic response—analyses and experiments. In *Proceedings of the 34th Aerospace Sciences Meeting and Exhibit*, Reno, Nevada. AIAA Paper 96-0014.

PATIL, M. J. & HODGES, D. H. 1998a Nonlinear aeroelasticity and flight dynamics of aircraft in subsonic flow. In *Proceedings of the 21st Congress of International Council of the Aeronautical Sciences*, Melbourne, Australia. AIAA Paper A98-31713.

PATIL, M. J., HODGES, D. H. & CESNIK, C. E. S. 1998b Nonlinear aeroelastic analysis of aircraft with high-aspect-ratio wings. In *Proceedings of the 39th Structures, Structural Dynamics, and Materials Conference*, pp. 2056–2068, Long Beach, CA. AIAA Paper 98-1955.

PATIL, M. J., HODGES, D. H. & CESNIK, C. E. S. 1999 Nonlinear aeroelasticity and flight dynamics of high-altitude long-endurance aircraft. In *Proceedings of the 40th Structures, Structural Dynamics and Materials Conference*, pp. 2224–2232, Saint Louis, Missouri, AIAA Paper 99-1470. (To appear in *Journal of Aircraft*)

PETERS, D. A. & JOHNSON, M. J. 1994 Finite-state airloads for deformable airfoils on fixed and rotating wings. In P. P. Friedmann & C. I. Chang (eds.) *Aeroelasticity and Fluid/Structure Interaction*, Vol. 44, pp. 1–28. New York: ASME.

PETERS, D. A., KARUNAMOORTHY, S. & CAO, W.-M. 1995 Finite state induced flow models; Part I: two-dimensional thin airfoil. *Journal of Aircraft* **32,** 313–322.

TANG, D., CONNER, M. D. & DOWELL, E. H. 1998 Reduced-order aerodynamic model and its application to a nonlinear aeroelastic system. *Journal of Aircraft* **35,** 332–338.

TANG, D. M. & DOWELL, E. H. 1993 Experimental and theoretical study for nonlinear aeroelastic behavior of a flexible rotor blade. *AIAA Journal* **31,** 1133–1142.